

# Interpolation of surface radiative temperature measured from polar orbiting satellites to a diurnal cycle

## 2. Cloudy-pixel treatment

Menglin Jin

Department of Atmospheric Sciences, University of Arizona, Tucson

**Abstract.** Global skin temperature is very important for the understanding of surface climate and for evaluating climate models. However, when the surface is obscured by clouds, this variable cannot be measured directly by using satellite thermal infrared channels. Methods for calculating skin temperature for a satellite cloudy pixel are important, yet little research on their relative merits has been done. The “cloudy-pixel treatment” presented here is a hybrid technique of “neighboring-pixel” and “surface air temperature” approaches. The neighboring-pixel approach (NP) for calculating skin temperature for a satellite cloudy pixel is described and tested against field experiments and climate model CCM3/BATS simulations. This approach is based on the surface energy balance with the soil heat flux being treated by a conventional force-restore method for bare soil and short vegetated surfaces, where ground heat flux is important. For other surfaces where soil heat flux is less important, for example, the fully vegetated forests in temperate and tropical regions, observed empirical relationships between solar radiative energy and skin temperature (i.e.,  $\Delta S_n/\Delta T_s$ ) are used. In addition, a “surface air temperature ( $T_a$ ) adjustment” is developed from the Monin-Obukhov similarity theory to infer skin temperature from 2-m air temperature using a knowledge of wind speed, pressure, boundary layer stability, and other surface properties. This adjustment is useful wherever surface air temperatures are available to insure the skin temperature consistency during daytime and nighttime. Error analyses show that this cloudy-pixel treatment has an accuracy of 1°–2° K at monthly mean pixel level resolution. This accuracy varies with season and vegetation type. Despite the uncertainty in this algorithm, this work can be practically used to calculate skin temperature for a cloudy pixel.

## 1. Introduction

Monitoring, understanding and, predicting land-atmosphere interactions related to global change require better data sets of land surface parameters governing energy, mass, and momentum exchanges between land and atmosphere. The surface skin temperature is important, in particular, because it represents the integrated features of land-atmosphere physical and dynamic processes. Obtaining an up-to-date global land surface skin temperature data set clearly requires the use of remote sensing by satellite. Instruments on polar orbiting satellites, such as advanced very high resolution radiometer (AVHRR) or Moderate-Resolution Imaging Spectrometer (MODIS) in the near future, have been playing an important role on the basis of their thermal channel measurements at the atmospheric window wavelength. Unfortunately, such satellite measurements, before they can be adequately used, have to be improved because of two limitations: the diurnal cycle of surface temperature cannot be obtained by a polar orbiting satellite because this kind of satellite passes a given area usually only twice a day; and no surface temperature can be measured for cloudy pixels because the clouds absorb the surface emission.

In a preceding paper, *Jin and Dickinson* [1999] present a method for interpolating satellite skin temperatures to diurnal

cycles and the applications of that method to “cloud-free” conditions. That algorithm, for the first time, interpolated satellite twice-daily observations to diurnal land surface skin temperature with an accuracy of 1–2 K at monthly pixel resolution. However, the *Jin and Dickinson* paper treated only clear-sky cases. This paper deals with cloudy-sky cases.

Obtaining skin temperature for a cloudy pixel is particularly important because cloudy-sky conditions represent more than half of the actual day-to-day weather and because the cloud cover, once present, significantly modifies the surface energy budget. Most of the work already accomplished in remote sensing retrieves brightness skin temperature from satellite-based near-infrared irradiance [*Price*, 1984; *Becker and Li*, 1990; *Parata et al.*, 1995; *Wan and Dozier*, 1996]. When the surface is overcast, the actual retrieved temperature for the corresponding pixel is, or is contaminated by, the cloud top temperature. This is because clouds absorb the surface long-wave radiation and emit it at a lower temperature. A search of the literature shows that few efforts have been made to derive surface skin temperature under cloudy sky (i.e., for cloudy pixels). So far, both *Minnis and Harrison* [1984] and *Minnis et al.* [1990] used nearby pixels, time interpolation, and air/surface temperature relationships to derive surface temperature pixels. These methods, however, only tested over small areas, and influences of surface vegetation/soil properties on temperature were not considered. The ISCCP algorithm uses cumulative clear-sky surface temperature as its nearby cloudy-pixel temperature (W. Rossow, personal communication,

Copyright 2000 by the American Geophysical Union.

Paper number 1999JD901088.  
0148-0227/00/1999JD901088\$09.00

1999). The aim of this work is to develop an effective way to integrate Earth Observing System (EOS) data to derive skin temperature with global coverage and high resolution. This skin temperature data set can be used to improve the accuracy of global climate models through more implicit modeling of surface-temperature-related land processes.

Surface skin temperature ( $T_s$ ) changes occur when clouds are present. One straightforward way to calculate  $T_s$  for a cloudy pixel is first to determine the relationships between cloud information and  $T_s$ , then to use satellite-provided cloud information to derive  $T_s$ . This method, however, is not practical at the current stage of research because there is a lack of understanding of the complex relationships between clouds and  $T_s$  and because adequately accurate cloud information cannot be obtained from the satellites so far.

Another method for deriving surface skin temperature is from the surface energy balance equation (SEB) by writing out the surface-related energy components in terms of  $T_s$ . The net effect of clouds on surface radiation is a difference of two large terms: a decrease in surface insolation and an increase in downward longwave radiation. Although the magnitude (and even the sign) of this net effect is controversial at the global scale, it is known to be a function of cloud type and cloud vertical distribution [Cess *et al.*, 1989; Ockert-Bell and Hartmann, 1992]. Regardless of the uncertainty in the net effect, the surface radiation amount and balance are dependent on the sky condition. Over the land surface, the SEB is

$$G = S_n - F_n - SH - LE, \quad (1)$$

where  $G$  is the ground heat flux,  $S_n$  is the net solar radiation at the surface,  $F_n$  is the net longwave radiation,  $SH$  is the sensible heat flux, and  $LE$  is the latent heat flux. If  $R_n$  is the net radiative energy at surface,

$$S_n = S_\downarrow - S_\uparrow, \quad (2)$$

$$F_n = F_\downarrow - F_\uparrow, \quad (3)$$

$$R_n = S_n - F_n, \quad (4)$$

where  $S_\downarrow$  and  $F_\downarrow$  are the downward fluxes and  $S_\uparrow$  and  $F_\uparrow$  are the upward fluxes. The upward longwave radiation ( $F_\uparrow$ ), sensible heat flux ( $SH$ ), and latent heat flux ( $LE$ ) are functions of skin temperature; that is,

$$F_\uparrow = \varepsilon \sigma T_s^4, \quad (5)$$

$$SH = \rho c_p C_{DH} U (T_s - T_a), \quad (6)$$

$$LE = L_v \rho C_{DE} U (q_*(T_s) - q_a), \quad (7)$$

where  $\varepsilon$  is surface emissivity,  $\sigma$  is the Stefan-Boltzmann constant,  $\rho$  is air density at surface layer,  $c_p$  is specific heat at constant pressure,  $L_v$  is latent heat, and  $C_{DH}$  and  $C_{DE}$  are transfer coefficients for heat and water vapor, respectively.  $U$  is wind speed at reference level,  $q_*(T_s)$  is specific humidity at  $T_s$ ,  $T_a$  is air temperature, and  $q_a$  is specific humidity at a reference level. With knowledge of surface and atmospheric conditions, such as  $T_a$ ,  $q_*(T_s)$ ,  $U$ , and  $q_a$ , skin temperature can be derived on the basis of the surface energy balance condition. Since these surface variables cannot be measured by satellite, this method needs more work before satellite data can be used alone to derive skin temperature.

Alternatively, a hybrid technique of “neighboring-pixel approach” (i.e., NP approach) and “air temperature adjustment”

(i.e.,  $T_a$  adjustment) is presented in this paper. The NP approach uses a cloudy-pixel skin temperature from its neighboring clear pixel skin temperature, net solar radiation ( $\Delta S_n$ ), net longwave radiation ( $\Delta F_n$ ), and net heat flux ( $\Delta SH$ ,  $\Delta LE$ ) differences between the two neighboring pixels. Since only  $\Delta S_n$  can be derived from the satellite measurements, and  $\Delta F_n$ ,  $\Delta SH$ , and  $\Delta LE$  are unknown variables, the climatological relationships between  $\Delta S_n$  and  $\Delta F_n$ ,  $\Delta SH$ ,  $\Delta LE$  are used to derive the unknown flux information as one possible approximation. Since middle- and high-latitude synoptic cloud systems typically extend hundreds to thousands of kilometers, a clear neighboring pixel may be difficult to find. The  $T_a$  adjustment is suggested as a supplement to the NP approach. This method is based on the Monin-Obukhov similarity theory and is used to calculate cloudy-pixel  $T_s$  from the above air temperature. This supplement is also used for the night cases. However, the  $T_a$  adjustment is limited by the requirement of surface measurements, which can be obtained only at weather stations. Because of the high heterogeneity of land surfaces, the surface measurements can represent only a small area. Therefore the  $T_a$  adjustment can best be used over the areas where the  $T_a$  are measured.

The rest of this paper is divided into six parts. The first section describes data used in this work. The second section summarizes both the neighboring-pixel approach and its supplement, the  $T_a$  adjustment algorithm. The third section discusses the application of the NP approach. The fourth section presents the evaluations of the algorithm using observations and GCM simulations. Error analyses are given, and finally, discussions and conclusions are presented.

## 2. Data

Both field experiment observations and climate model simulations have been used to validate the algorithm. The observed flux data illustrate the relationships among the surface energy terms ( $F_n$ ,  $S_{nle}$ , and  $S_n$ ). Model simulations validate the relationships obtained in observations over other areas. Skin temperature measurements from both FIFE and BOREAS are used to test the algorithms.

### 2.1. Data From Field Experiments

There are six field experiments used in this work. They cover various surface types, including shortgrass (FIFE, Cabauw, ARM), temperate forest (BOREAS), soya bean (HAPEX), midlatitude mountains (SURFRAD), desert (SURFRAD), and creek (SURFRAD).

The measurements of surface fluxes and skin temperatures from FIFE [Sellers *et al.*, 1992] and BOREAS [Sellers *et al.*, 1995] field experiments, as used by Jin and Dickinson [1999], are again used in this paper.

SURFRAD is a field project conducted by the Surface Radiation Research Branch (SRRB) of the NOAA Air Resources Laboratory. This project provides quality surface radiation measurements. Currently, there are six stations over the United States which cover agriculture, mountain, and desert surface types. The SURFRAD station in Bondville is located in an agricultural region about 10 miles southwest of Champaign, Illinois. The Boulder SURFRAD instruments are located on the deck at the SRRB Table Mountain Test Facility, located 8 miles north of Boulder. The Desert Rock SURFRAD station is located at the Desert Rock (DRA) operational radiosonde station on the Nevada Test Site, 65 miles

northwest of Las Vegas. The Fort Peck, Montana, station is located on the Fort Peck Tribes Reservation, ~15 miles north of Poplar, Montana. The Goodwin Creek SURFRAD station is located on rural pasture land about 20 miles west of Oxford, Mississippi. The Pennsylvania State University SURFRAD station is located on the grounds of the PSU agricultural research farm.

Two forcing data sets employed in the Project for Intercomparison of Land-Surface Parameterization Schemes (PILPS), Stage II, have been used here. Data of surface energy terms are measured from the site of Caumont of HAPEX-Mobilhy. The site is located at 43.41°N, 0.06°W with vegetation type being a crop of soya. Cabauw data are provided by the Royal Netherlands Meteorological Institute for a shortgrass area [Beljaars and Bosveld, 1994].

Forcing data from Atmosphere Radiation Measurement (ARM) have also been used to examine the single-column CCM3 model (SCCM) simulation [Randall and Wielicki, 1997]. The consistency between observations and model results is the basis for the use of SCCM in this study.

## 2.2. Data From Model Simulations

Field experiments cover only selected surface types and locations, so model simulations are necessary to study other areas. The NCAR CCM3 climate model coupled with BATS has been used to examine the relationship among energy exchanges and to evaluate the algorithm with the hourly model simulations that were used by Jin and Dickinson [1999].

The single-column CCM3 model (SCCM) has been used to study surface energy exchanges for one column. SCCM serves as a supplement to CCM3/BATS because the GCM has much coarser resolution (~250 km × 250 km) than that of a satellite. At such large resolution, some subgrid physical processes and interactions related to skin temperature may not be well simulated in CCM3/BATS. SCCM is also better for examining the physical process with less computational expense than that of the CCM3 itself. Comparing the SCCM results with ARM, FIFE, and BOREAS measurements provides an assessment of the simulation abilities of both SCCM and CCM3/BATS.

## 3. Methodology

### 3.1. Neighboring-Pixel Approach (NP Approach)

**3.1.1. Technique.** The term neighboring is used in either the spatial or the temporal sense in this work. For a cloudy pixel, the “neighboring clear pixel” means a clear pixel over similar vegetation, soil, and topographic conditions and within a certain latitude or longitude distance. This ensures that the temperature differences between these clear and cloudy pixels are caused primarily by different cloud conditions.

Since the detailed surface energy distribution is unknown, skin temperature of a pixel cannot be derived from its surface energy budget alone. The NP approach is based on the understanding that clouds change radiative energies that reach the surface and, consequently, modify the surface skin temperature. In other words, the temperature difference between two neighboring pixels ( $\Delta T_s$ ) is mainly caused by their different radiation input and redistribution. Figure 1 presents the schematic diagram of the NP approach. For a cloudy pixel  $i(t)$  at time  $t$ , assuming that the skin temperature for its neighboring clear pixel  $j(t)$  and previous day pixel  $i(t-1)$  are available,  $T_s^{j(t)}$  and  $T_s^{i(t-1)}$ ,  $T_s^{i(t)}$  can be related to  $T_s^{j(t)}$  and  $T_s^{i(t-1)}$  through the surface energy balance equation.

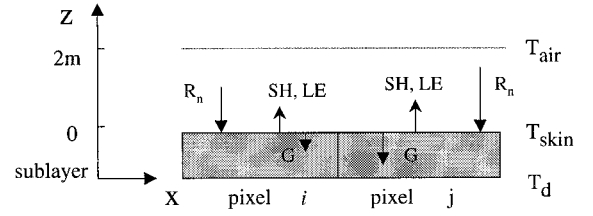


**Figure 1.** Schematic diagram of the neighboring-pixel approach with a thin subsurface that has temperature  $T_d$ . The surface has skin temperature  $T_s$ , and the air temperature ( $T_a$ ) is observed at 2 m above surface.

From (1), if  $S_{hle}$  is the sum of  $SH$  and  $LE$ , and each energy term can be connected to  $T_s$ ,

$$\frac{\partial G}{\partial T_s} = \frac{\partial S_n}{\partial T_s} - \frac{\partial F_n}{\partial T_s} - \frac{\partial S_{hle}}{\partial T_s}. \quad (8)$$

Note that  $\partial \Delta S_n / \partial T_s$  does not mean the net solar radiation is a function of  $T_s$ . This mathematical expression is valid only because  $S_n$  is equal to the  $T_s$ -related energy terms; that is,  $S_n = G + F_n + S_{hle}$ .

On the basis of the conventional force-restore method [Deardorff, 1978; Dickinson, 1988],

$$G = k_g \frac{\partial T}{\partial Z} = k_g \frac{(T_s - T_d)}{\Delta Z}, \quad (9)$$

where  $T_d$  is the sublayer temperature,  $k_g$  is thermal molecular conductivity of ground soil in units  $\text{W m}^{-2} \text{K}^{-1}$ , and  $\Delta Z$  is the depth of subsurface layer. Observations show that the sublayer temperature  $T_d$  is much less sensitive to surface insolation [Stull, 1988] than the skin temperature. Therefore for two adjacent pixels,

$$\frac{\partial G}{\partial T_s} = \frac{\partial}{\partial T_s} \left[ k_g \frac{(T_s - T_d)}{\Delta Z} \right] \approx \frac{k_g}{\Delta Z}. \quad (10)$$

In addition,

$$\frac{\partial S_{hle}}{\partial T_s} \approx \frac{\Delta S_{hle}}{\Delta T_s} = \frac{\Delta S_{hle}}{\Delta S_n} \frac{\Delta S_n}{\Delta T_s}, \quad (11)$$

$$\frac{\partial F_n}{\partial T_s} \approx \frac{\Delta F_n}{\Delta T_s} = \frac{\Delta F_n}{\Delta S_n} \frac{\Delta S_n}{\Delta T_s}. \quad (12)$$

Combining (10), (11), and (12),

$$\Delta T_s = \frac{\Delta Z}{k_g} (\Delta S_n - \Delta F_n - \Delta S_{hle}), \quad (13)$$

$$\Delta T_s = \frac{1}{\lambda} (1 - a - b) \Delta S_n = \frac{1}{K} \Delta S_n, \quad (14)$$

or

$$T_s^i = T_s^j + \frac{1}{K} \Delta S_n^j, \quad (15)$$

where  $\lambda = k_g / \Delta Z$ ,  $a = \Delta F_n / \Delta S_n$ ,  $b = \Delta S_{hle} / \Delta S_n$ , and  $\frac{1}{K} = (1 - a - b) / \lambda$ . Both  $a$  and  $b$  depend on surface type. A later section will discuss how to obtain  $a$  and  $b$ . Equation (14) or (15) is the generally used NP approach format. In (15),  $T_s^i$  stands for the cloudy pixel, and  $T_s^j$  stands for the neighboring pixel, either spatial neighboring  $T_s^{j(t)}$  or temporal neighboring

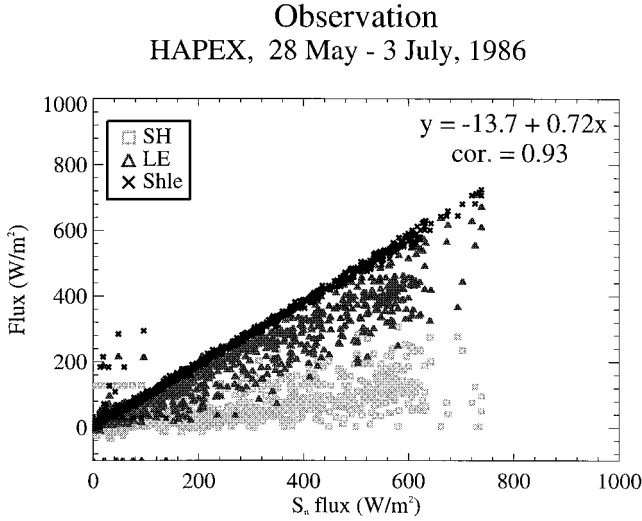


**Figure 2.**  $SH$ ,  $LE$ , and  $S_{hle}$  fluxes versus  $S_n$ . Data are observed over the HAPEX experiment in 1986 and have 30-min intervals.

$T_s^{i(t-1)}$  or the sum of them.  $\Delta S_n^j$  is the difference of net solar radiation between pixels  $i$  and  $j$ .

For a given cloudy pixel, very possibly, there may be more than one neighboring clear pixel. The noncoincidence in time and place of the neighboring pixels may have different contributions in inferring the cloudy-pixel skin temperature. In other words, the spatially or temporally neighboring pixels  $T_s^j$  may have different weights for the cloudy-pixel skin temperature  $T_s^i$ . If each clear pixel has weight  $w_j$ , (15) can be restated as

$$T_s^i = \frac{1}{N} \sum_{j=1}^N w_j T_s^j + \frac{1}{N} \sum_{j=1}^N w_j \lambda \Delta S_n^j + d', \quad (16)$$

where  $\sum_{j=1}^N w_j = N$ , and  $d'$  is the residual uncertainty.

**3.1.2. Sum of sensible and latent heat fluxes.** In this work,  $SH$  and  $LE$  are treated as one term,  $S_{hle}$ , because knowing the detailed partitioning between these fluxes is beyond the scope of this work and because the sum,  $S_{hle}$ , is more closely related to the solar radiation than is each of the individual fluxes [Betts *et al.*, 1996; Betts and Ball, 1995]. Figure 2 shows the scatterplot for net solar radiation versus  $LE$ ,  $SH$ , and  $S_{hle}$ , respectively. Data are measured over the HAPEX area during the period May 28 through July 3, 1986. The sum of the heat fluxes increases with  $S_n$  more monotonically than either the sensible or the latent flux. The relationship between  $S_{hle}$  and  $S_n$  can then be well described using a linear regression equation (given at the top right-hand corner of Figure 2), suggesting that the fraction of  $S_n$  transferred into heat fluxes is almost constant in July over the HAPEX experiment field. In other words,  $\Delta S_{hle}/\Delta S_n$  is statistically uniform. For different surface types this fraction may differ, but it remains relatively constant for a given type.

**3.1.3. Calculation of  $k_g$ .** If there are no energy sinks and sources in the soil, according to the second thermodynamic law, we have the following simple prognostic equation:

$$\frac{\partial T}{\partial t} = -\frac{1}{c_g} \frac{\partial Q}{\partial Z}, \quad (17)$$

where  $c_g$  is soil heat capacity (i.e., soil density multiplied by specific heat) in units  $\text{J m}^{-3} \text{K}^{-1}$ . If  $Q_g$  is the flux transported in the soil,

$$Q_g = -k_g \frac{\partial T}{\partial Z}. \quad (18)$$

Combining (17) and (18), we obtain

$$\frac{\partial T}{\partial t} = \nu_g \frac{\partial^2 T}{\partial Z^2} \quad (19)$$

as the transport equation, with  $\nu_g$  the soil diffusivity in  $\text{m}^2 \text{s}^{-1}$ . The relationship of  $\nu_g$ ,  $c_g$ , and  $k_g$  is

$$\nu_g = \frac{k_g}{c_g}. \quad (20)$$

Soil thermal conductivity ( $k_g$ ), diffusivity ( $\nu_g$ ), and heat capacity ( $c_g$ ) depend on surface type, soil moisture, and soil texture. From an Amazon rain forest experiment, the value of  $k_g$  is 0.113 for the dry case and 11.06 for the wet case [Shuttleworth, 1989]. Table 1 is adapted from Stull [1988] for some measured soil conductivities. We copied the method of calculating  $k_g$  from BATS, i.e., for nonfrozen bare soil,

$$\nu_g = \frac{(2.9\rho_w + 0.04)k_c}{(1 - 0.6\rho_w)\rho_w + 0.09}, \quad (21)$$

$$k_c = 10^{-7} \text{ m}^2 \text{ s}^{-1} \times R_{AT}, \quad (22)$$

where  $R_{AT}$  is the ratio of the thermal diffusivity for a given texture to that for loam, and  $\rho_w$  is the volume of liquid water per unit volume of soil, i.e., soil water density. Both  $R_{AT}$  and  $\rho_w$  can be obtained from the BATS parameterization [Dickinson *et al.*, 1993, Table 3, equation (39)].

Our research shows that this method gives reasonably accurate thermal conductivities. For example, the calculated  $k_g$  for a saturated FIFE area is about  $0.9 \text{ W m}^{-1} \text{ K}^{-1}$ , and for a BOREAS forest area, it is  $1.56 \text{ W m}^{-1} \text{ K}^{-1}$ , which are consistent with observations.

**3.1.4. Determination of  $K$ .** According to (13) and (14),  $\frac{1}{K} = (1 - a - b)/\lambda$ , where  $\lambda = k_g/\Delta Z$ .  $\Delta Z$  is the soil depth where no diurnal temperature can be significantly observed,

**Table 1.** Soil and Ground Properties (Letau, personal communication) Where  $\rho$  = Density ( $\text{kg m}^{-3}$ ),  $C$  = Volumetric Heat Capacity ( $10^6 \text{ J m}^{-3} \text{ K}^{-1}$ ),  $\nu$  = Thermal Diffusivity ( $10^{-6} \text{ m}^2 \text{ s}^{-1}$ ), and  $k_g$  = Thermal Conductivity ( $\text{W m}^{-1} \text{ K}^{-1}$ )

Type	Composition	$\rho$	$C$	$\nu$	$k_g$
Quartz sand	dry	1500	1.24	0.24	0.33
	10% moisture	1650	1.54	1.22	1.88
	40% moisture	1950	2.76	0.91	2.51
Sandy clay	15% moisture	1780	2.42	0.38	0.92
Swamp land	90% moisture	1050	3.89	0.23	0.89
Rocks	basalt	2800	2.34	0.66	1.54
	sandstone	2600	2.30	1.13	2.60
	granite	2700	2.13	1.28	2.73
	concrete	2470	2.26	1.08	2.44
Snow	new feathery	100	0.21	0.10	0.02
	old packed	400	0.84	0.40	0.34
	ice	920	2.05	0.92	1.89
Water	still	1000	4.18	0.14	0.59

Adapted from Stull [1988, Table C-8].

and physically, this depth is up 0.1 m for different soil types. Coefficients  $a$  and  $b$  can be inferred from section 4.2. For example, over BOREAS,  $a$  is around 0.06 and  $b$  is around 0.80, and  $\Delta Z$  could be shallow as a normal soil type, say 0.08–0.1 m, and  $k_g$  from the previous section is  $1.56 \text{ W m}^{-1} \text{ K}^{-1}$ , therefore  $K$  has a value of about  $130\text{--}150 \text{ W m}^{-2} \text{ K}^{-1}$ . For simplicity, in this work, we choose  $K$  as  $140 \text{ W m}^{-2} \text{ K}^{-1}$ .

**3.1.5. Full vegetation.** The role of vegetation is principally to modify the amount of surface energy available from radiative input and to determine the partitioning of that energy between the fluxes of energy into the soil and, in latent and sensible heat forms, into the atmosphere. Because of the significant influences of vegetation cover on surface energy exchanges, forest areas have a different equation governing surface energy and thus need to be considered separately from bare soil areas.

Over fully vegetated areas, for example, the tropical and temperate forests, the surface energy budget is more complex because of the interception of radiation by the vegetation layer and because of the heat stored by the canopy and the air between the top canopy and the soil [Shuttleworth, 1989]. In general, the forest has

$$G = R_n - S_{hle} - \Delta S, \quad (23)$$

where  $\Delta S$  is the storage term from vegetation and air between the canopy top and the surface. The midday  $\Delta S$  for the Amazonian forest is measured as  $30\text{--}40 \text{ W m}^{-2}$  or less [Bastable *et al.*, 1993] and, consequently, can be ignored as a close approximation [Garratt, 1992].  $G$  is also small because radiant energy is intercepted before reaching the ground [Shuttleworth, 1989]. Thus

$$S_n = F_n + S_{hle}. \quad (24)$$

Similar to (14),

$$K = \frac{\Delta S_n}{\Delta T_s}. \quad (25)$$

Because of the lack of understanding of the dynamics and interactions among the atmosphere, vegetation cover, and soil layer, it is very difficult to calculate  $K$  for forest areas. In this work, values of  $K$  for the forest areas are inferred from observations and examined by model simulations. The physical meaning of  $K$ , or  $\Delta S_n/\Delta T_s$ , relates to the interactions of surface climate systems and the feedbacks among them [Cess, 1976; Lian and Cess, 1977; Ramanathan, 1987]. For BOREAS in July, the  $K$  obtained from observations approximates  $140 \text{ W m}^{-2} \text{ K}^{-1}$ , which is consistent with section 3.1.4. Further studies show this value does not vary much with season, indicating that the response of temperature to radiative input is almost the same during the entire year over forest areas.

### 3.2. $T_a$ Adjustment

Clouds occur under two different dynamic mechanisms: local convection or synoptic advection. In the latter, clouds horizontally cover from hundreds to thousands of kilometers and usually last several days. Thus the neighboring pixel approach might not work well because of the difficulty in finding a neighboring “clear” pixel spatially and temporally. Furthermore, although it is generally true that for large-scale overcast regions the surface is rather neutral and surface skin temperature is close to that of the previous overcast day, the daily variability of atmospheric conditions (e.g., wind and precipita-

tion) may still cause a significant difference between the temperatures of two consecutive days. In such cases the NP approach may not be accurate; thus the air temperature adjustment becomes important.

$T_a$  (or “screen air” temperature) is the temperature at 1.5–2 m above the land surface. This temperature is closely related to skin temperature because of the energy transported through convection, conduction, and radiation [Jin *et al.*, 1997]. Since these three processes are fundamentally different, the relationship between  $T_s$  and  $T_a$  is difficult to describe using one simple formula. A good estimate of this relationship can be inferred from the boundary layer Monin-Obukhov similarity theory for the potential temperature profile [Garratt, 1992, chapter 3]. Details are given in the Appendix.

The advantage of the  $T_a$  algorithm is that one can calculate skin temperature of the cloudy pixel from air temperature. The disadvantage is that the traditional Monin-Obukhov surface layer theory was developed over homogeneous terrain, thus this method, in principle, is valid only for homogeneous surfaces. Since  $T_a$  is measured only at weather stations, then in practice, this method can be applied only where surface measurements are available. However, this method can be used as a supplement to the foregoing neighboring-pixel method to improve the skin temperature accuracy over  $T_a$ -available regions.

## 4. Discussion of the NP Approach

Before this NP approach, in the form of (16), can be used on a satellite data set, several problems need to be addressed: (1) how to determine the weight for different clear pixels, (2) how to determine  $\Delta F_n$  and  $\Delta S_{hle}$ , and (3) how to treat the bias term  $d'$ .

### 4.1. Determine Weights

The weight of each neighboring pixel depends on its distance from the cloudy pixel and the consistency of the skin temperature field. Weights represent relationships of different pixels to the cloudy pixel. Autocorrelation illustrates the persistence or the tendency for data in time or space and thus can be used to describe the contribution of each neighboring pixel to the cloudy pixel. A similar method has been used by Minnett [1991] for sea surface temperature. His work found that a spatial separation of about 10 km and time intervals of about 2 hours can introduce an rms difference of 0.2 K into the error budget of a satellite data set. However, although Minnett’s work sheds light on our problem, his results cannot be directly adopted here because the temporal pixels used here are at 24-hour intervals, instead of 1 hour, and because the land surface is much more complex than the sea surface. More importantly, the proposed NP approach uses not only the temperatures of the neighboring clear pixels but also the  $\Delta S$  information.

To determine the weight of temperatures measured at the same overpass time but on different dates, the FIFE site-averaged observations, in July 1988, were analyzed. There were 31 skin temperatures measured at 1000 LT during that month (Figure 3a). The corresponding net solar radiation at the surface is given in Figure 3b. Figure 3c is the algorithm-produced skin temperature using the previous 2-day measurements and (16). The previous two days are treated equally. The solid line in Figure 3d is the autocorrelation of the  $T_s$  shown in Figure 3a, and the dashed line is for the calculated  $T_s$  shown in Figure 3c. The autocorrelation coefficients significantly decrease with larger autocorrelation lags in terms of day. The differences

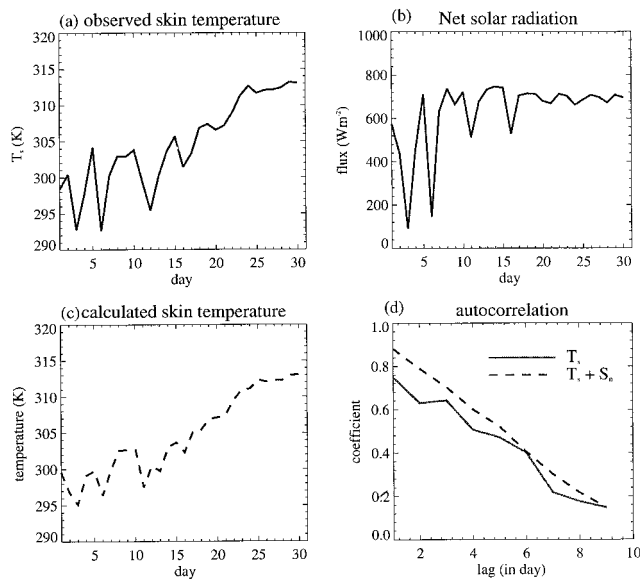


**Figure 3.** Temporal autocorrelation analysis using FIFE observations of July 1988. (a) Observed skin temperature for each day at 1000 LT. (b) Net solar radiation for each day at 1000 LT. (c) Algorithm-calculated skin temperature based on equation (16). Previous day skin temperature and the net solar radiation are used in calculation, as shown in (16). (d) Autocorrelation coefficient as a function of lag in days. The solid line is based on Figure 3a, and the dashed line is based on Figure 3c.

between the solid and the dashed lines in Figure 3d show that after including solar radiation the autocorrelation improves monotonically. For lag = 1 day and lag = 2 days, autocorrelation coefficients are as high as 0.8 (dashed line), implying that the previous 2-day temperatures have a high persistence with the more distant days. This suggests that the previous one and two days can be treated equally by the NP algorithm, for acceptable accuracy and simplicity. Information from the more distant days is also useful but less significant than that for the previous 1–2 days in retrieving skin temperature of the cloudy pixel.

It is difficult to determine the spatial persistence of a surface temperature because of the lack of high spatial resolution data. However, the satellite-based temperatures, although contaminated by the clouds, still can provide some information on the persistence. GOES-7 infrared temperatures measured in July 1991 and provided by the ISCCP DX data sets are analyzed for this purpose. Figure 4a is the coverage of the GOES-7 data set. The spatial resolution of this data set is 30 km. We choose the IR temperatures along latitude 40°N and longitude 90°E, respectively. The temperatures are presented in Figures 4b and 4c; the extreme low values are the cloud top temperatures. The corresponding autocorrelations of the skin temperatures are given in Figures 4d and 4e, respectively. The autocorrelation coefficients reduce more rapidly along the latitude than along the longitude. Along longitude the autocorrelation is above 0.8 for the closest 10 pixels, corresponding to 300 km. This difference between latitude and longitude is caused by both the underlying surface conditions and the cloud distribution and thus may not be a general feature globally. However, it appears that spatial homogeneity may be assumed within a distance of about 3° of the cloudy pixel in the NP algorithm.

## 4.2. Parameterize $F_n$ and Heat Fluxes

The original formula of the NP algorithm, (13), requires knowledge of the net longwave radiation and the sensible and latent heat fluxes. One main problem is that  $\Delta F_n$  and  $\Delta S_{hlc}$  are not available from satellites. On the contrary,  $\Delta S_n$  can be derived from satellite remote sensing [Li *et al.*, 1993]. Since  $\Delta F_n$  and  $\Delta S_{hlc}$  are closely related to  $\Delta S_n$ , this work parameterizes  $\Delta F_n$  and  $\Delta S_{hlc}$  using  $\Delta S_n$ . Figures 5a, 5b, and 5c compare  $F_n$  with  $S_n$  over the FIFE area in July 1988, Fort Peck Mountain in July 1998, and the Penn State University station in July 1998; Figures 5d, 5e, and 5f are over the same station, Desert Rock, for different seasons. With the exception of Figure 5a, all other observations are from the SURFRAD project, 3-min averages of 1-s samples. The net longwave radiation increases with solar radiation, with simultaneous peaks and only small nocturnal variations. The maximum  $S_n$  has a magnitude from about 500  $\text{W m}^{-2}$  for full clouds to 1000  $\text{W m}^{-2}$  for a clear day.  $F_n$ , however, has a much smaller variation, from zero to 100  $\text{W m}^{-2}$  over normal surface and up to 200  $\text{W m}^{-2}$  at noon over desert areas. Compared to  $S_n$ , the diurnal variation of  $F_n$  is as small as 50–100  $\text{W m}^{-2}$ . This indicates that  $F_n$  plays a more moderate role in the surface energy balance than surface insolation. The linear regression equation is shown in the top right-hand corner for each panel. Other statistics also prove the significance of the linear regression relationships; for example, the standard deviations are 1.7 and 0.01 for intercept and slope of the regression equation in Figure 5a. The fractions of  $\Delta F_n$  to  $\Delta S_n$  differ with seasons but are within a small range, from 0.11 to 0.17.

To understand the extreme values observed over the desert, Figure 6 gives detailed information for one day in July 1998. Figure 6a shows  $F_n$  versus  $S_n$  and Figure 6b shows the diurnal variations of  $S_n$  and  $F_n$ , both as a function of time. The extreme values in Figure 6a are mainly caused by the short-time changes of sky conditions. The maximum  $S_n$  and  $F_n$  occur at almost the same time, near noon. The cloud effects on surface radiation are observed in both the  $S_n$  and the  $F_n$  fields, with the larger variation on  $S_n$  than on  $F_n$ . Another noticeable feature is the lag impact of  $S_n$ . Figure 6a has two branches: in general, the upper one corresponds to afternoon and the lower one to morning. For the same value of  $S_n$ , say 400  $\text{W m}^{-2}$ ,  $F_n$  were 180 and 120  $\text{W m}^{-2}$ , respectively. This is because  $F_n$  is influenced by the combined effects of clouds, water vapor, atmospheric temperature, and surface temperature. For the same  $S_n$  at morning and afternoon, the above conditions, in particular atmospheric and surface temperatures, are usually different and cause a different value of  $F_n$ . However, this feature does not change the fraction  $\Delta F_n/\Delta S_n$  because the slopes for the morning and afternoon branches are almost the same. At night, there is no solar radiation and  $F_n$  is almost constant.

The linear relationships between  $\Delta F_n$  and  $\Delta S_n$  are further examined over the other areas using general circulation model (GCM) simulations. Figures 7a–7d are the single-column CCM3 simulations of  $F_n$  versus  $S_n$  for BOREAS, Africa tallgrass area, Arizona desert, and ARM shortgrass area. Although the slopes of the regression equation may be a little different from those of the observations, the overall linear relationship between  $F_n$  and  $S_n$  is obvious. Consequently, a linear regression equation can describe such a relationship for a given surface,

$$F_n = a_0 + aS_n. \quad (35)$$

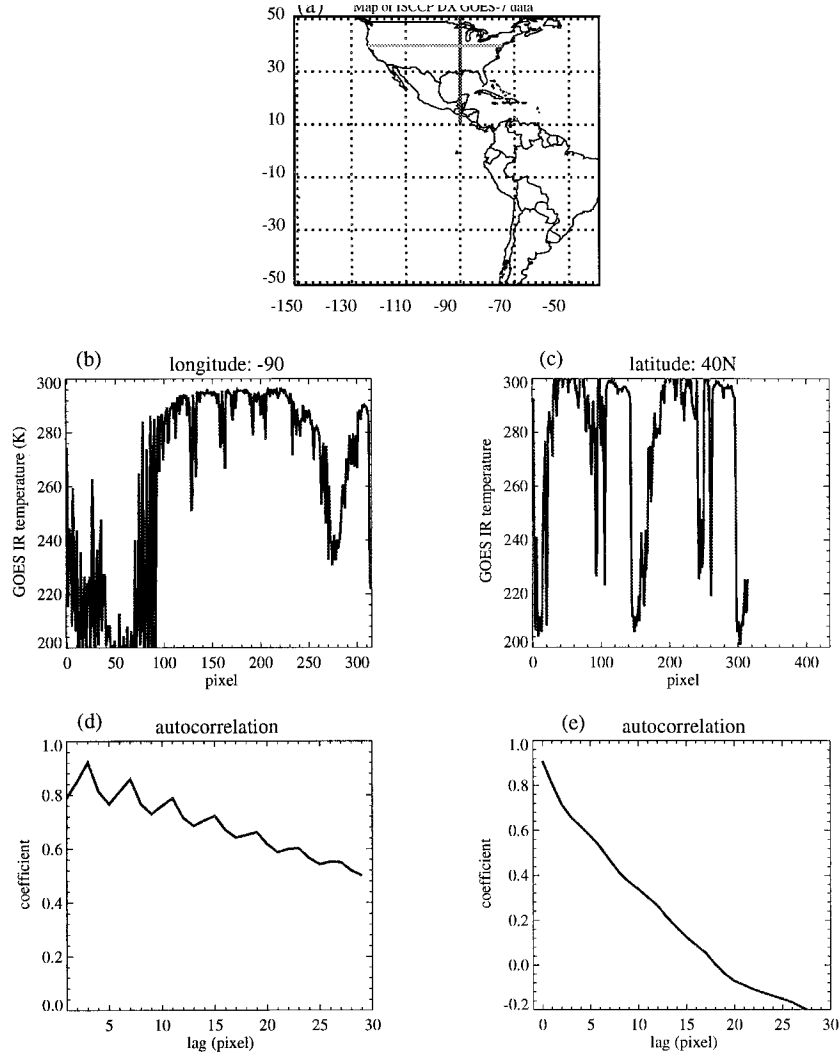


**Figure 4.** Spatial autocorrelation analysis using GOES-7 observations. The data are measured at 0000 UT, July 1, 1991. (a) Selected latitude (40°N) and longitude (90°E). (b) Temperature variation along the longitude (90°E), as shown in Figure 4a. (c) Same as Figure 4b but along the latitude (40°N). (d) Autocorrelation coefficient corresponding to Figure 4b. (e) Autocorrelation coefficient corresponding to Figure 4c.

The coefficients  $a_0$  and  $a$  are related to the surface properties and thus may vary with locations. If two neighboring pixels have similar surface properties and thus similar surface albedo, they hold the same coefficients,  $a_0$  and  $a$ . Therefore

$$\Delta F_n = a \Delta S_n. \quad (36)$$

The coefficient  $a$  is a function of surface soil properties and is generally smaller than 0.2, with 0.06 for forests to 0.15 for desert areas (Figure 7). This implies that less than 20% net solar radiation is balanced by net longwave radiation.

Similarly,  $S_{hle}$  can also be linked to  $S_n$ . Figure 8 compares  $S_{hle}$  versus  $S_n$  over various areas and seasons. Figure 8a is the observed FIFE area for July 1988; Figures 8b, 8c, and 8d are over Cabauw for January, May, and September, respectively. The two field experiments were conducted over the same surface type, shortgrass, but at different latitudes and seasons. Obviously,  $S_{hle}$  linearly relates to  $S_n$ . The linear regression equation for each season is at the right-hand top corner of each panel. The slopes vary with seasons but only within a small range, from 0.68 for winter to 0.76 for July. Comparing Figures

8b, 8c, and 8d, January and July seem to be the limits for this coefficient. Regardless of the intercept coefficient, the slope coefficient varies with season less than 10%. Similar relationships have also been demonstrated in other areas. For example, Figure 9 presents the relationships between  $S_{hle}$  and  $S_n$  over Africa, Arizona, ARM shortgrass, and BOREAS forest areas. The data are from CCM3 single-column model simulations for July. Therefore

$$S_{hle} = b_0 + b S_n, \quad (37)$$

and for two neighboring pixels,

$$\Delta S_{hle} = b \Delta S_n. \quad (38)$$

The coefficient  $b$  is a function of the local surface and soil properties. This coefficient may range from 0.44 for very dry desert to 0.78 for forest.

Note that the relationships presented here are statistical features. It is very possible that each day's  $F_n$  and  $S_{hle}$  may be different from the climatological status. Using such statistical

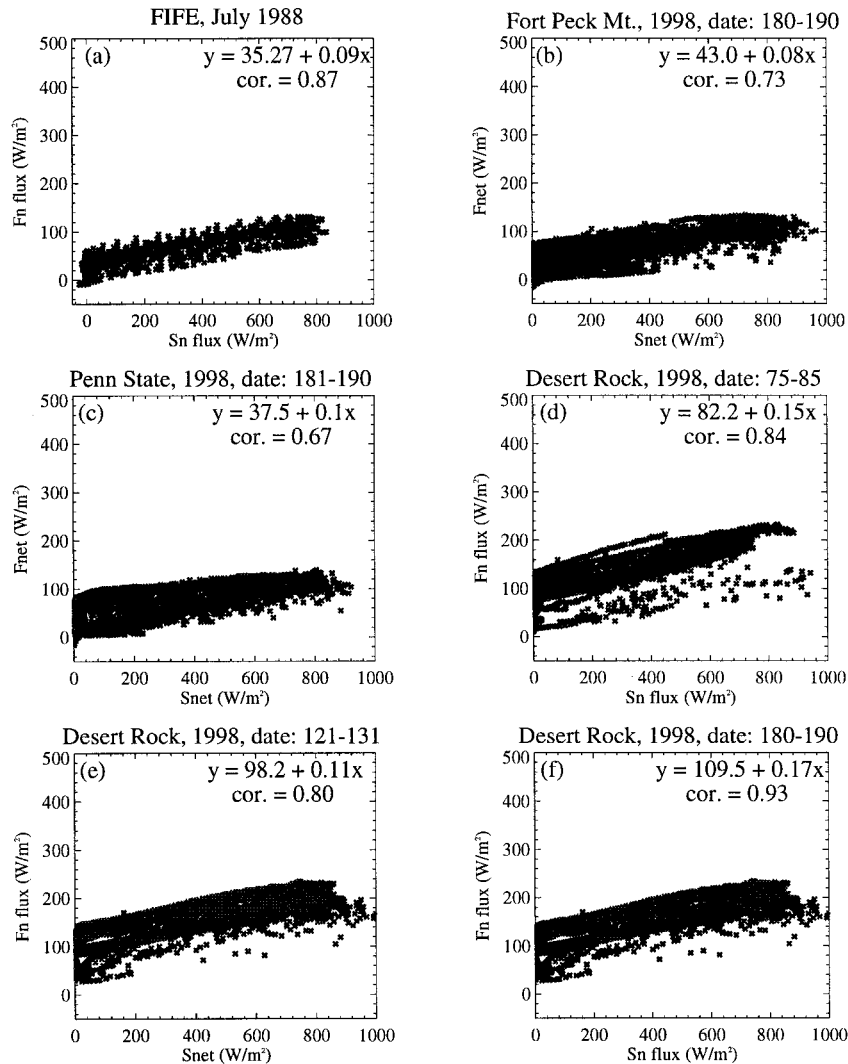


**Figure 5.** Net longwave radiative flux versus net solar radiative flux over (a) FIFE area for July 1988 (the data include all hourly measurements for site-averaged FIFE observations); (b) Fort Peck Mountain stations from SURFRAD project; (c) the Penn State University station from SURFRAD project; (d, e, f) Desert Rock station for Julian dates 75–85, Julian dates 121–131, and Julian dates 180–190, 1998, respectively.

relationships in the preceding NP approach may cause error. However, the statistical relations have captured most of the possible behavior of  $F_n$  and  $S_{hle}$  and thus could be used to describe each day's  $F_n$  and  $S_{hle}$  as a best guess when the actual measurements are not available. In addition, error analysis shows that the error resulting from such an approximation is acceptable. For example, in the ARM case, for the same amount of  $S_n$ ,  $S_{hle}$  may vary  $100 \text{ W m}^{-2}$ ; that is,  $\Delta S_{hle}$  is about  $100 \text{ W m}^{-2}$ . As shown in (13),  $\Delta S_{hle}$  has to be divided by  $K$  and causes a final error less than  $0.5^\circ \text{ K}$ .

#### 4.3. Determine $d'$

The  $d'$  is bias introduced by the approximation of net longwave radiation, approximation of sensible and latent heat fluxes, and the force-restore treatment on ground heat flux. For example, at night the sensible and latent heat fluxes are still unavailable but cannot be linked to the  $S_n$  since there is no surface insolation at night. As our research proved, during the day, the NP algorithm does not have a consistent sign of uncertainty, thus the bias  $d' = 0$ . On cloudy nights, skin tem-

perature is close to its air temperature and on clear nights over the FIFE area in summer, the air temperature is about  $2 \text{ K}$  greater than the skin temperature [Jin *et al.* 1997]. The  $d'$  here relates to the clear and cloudy skin temperature difference. For practical purposes we can assume  $d' = 2 \text{ K}$  at nights for the FIFE areas. In fact,  $d'$  depends on local surface and soil moisture properties and also depends on the real-time cloud conditions.

## 5. Results

### 5.1. Neighboring Pixel Approach

This section validates the NP approach against field experiments and the  $T_{42}$  CCM3/BATS simulations (i.e., about  $2.8^\circ \times 2.8^\circ$  resolution). The evaluations are implemented for daytime and nighttime separately because, for daylight hours, the temperature differences between clear and cloudy pixels are caused mainly by cloud influences on surface insolation. At night, however, the differences are due to the integrated ef-

fects of longwave radiation, sensible and latent fluxes, and soil flux. These different physical processes result in different accuracies for day and night.

For clear interpretation the algorithm, (16), is restated in terms of cloudy pixel  $i(t)$  and its neighboring pixels  $j(t)$  and  $i(t - 1)$ . The  $j(t)$  is the neighboring field station when possible, and  $i(t - 1)$  is the previous day of the  $i(t)$  station. The weights of these two pixels are considered to be equal, as discussed earlier.  $T_s^{i(t)}$  is the average of neighboring pixel skin temperatures plus flux correction terms  $\Delta S_n$ ,  $\Delta F_n$ , and  $\Delta S_{hle}$ ; that is

with flux corrections,

$$T_{skin}^{i(t)} = \frac{1}{2}(T_s^{i(t-1)} + T_s^{j(t)}) + \frac{1}{2K}(\Delta S_n - \Delta F_n - \Delta S_{hle}) + d'; \quad (39)$$

without flux corrections,

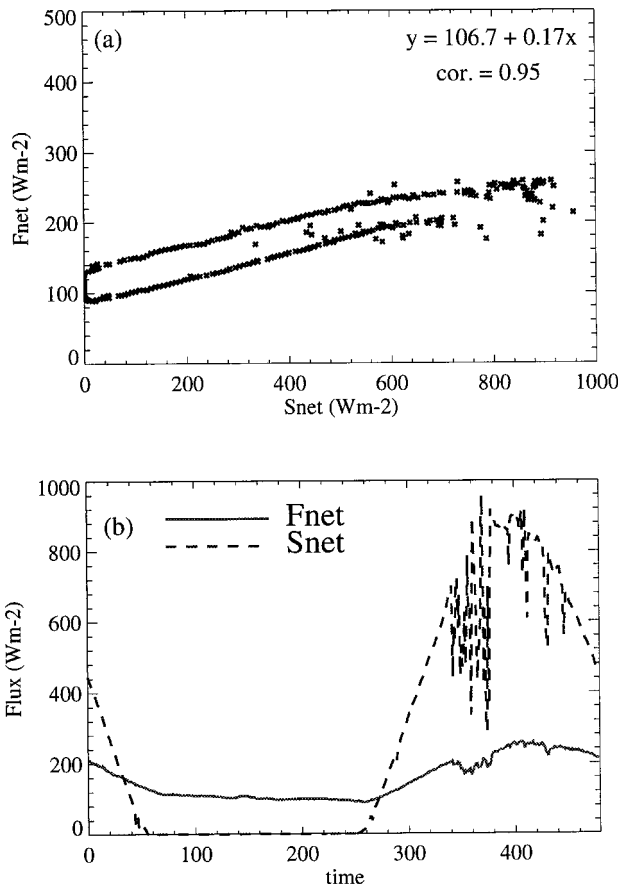
$$T_s^{i(t)} = \frac{1}{2}(T_s^{i(t-1)} + T_s^{j(t)}) + d', \quad (40)$$

where  $d' = 0$  for daylight hours, and  $d' > 0$  for nighttime hours.

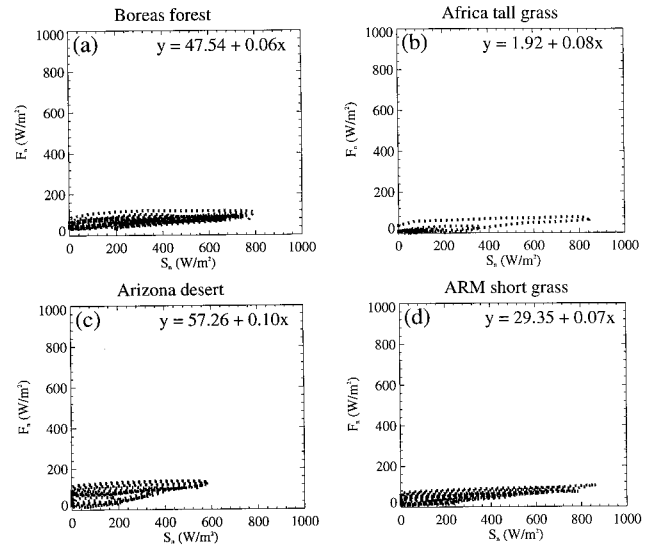
**5.1.1. Ground observations.** Figure 10 is a comparison of algorithm-produced skin temperatures with observations. The

### SURFRAD Observation

Desert Rock (36.63 -116.02), 1998, Julian date: 189

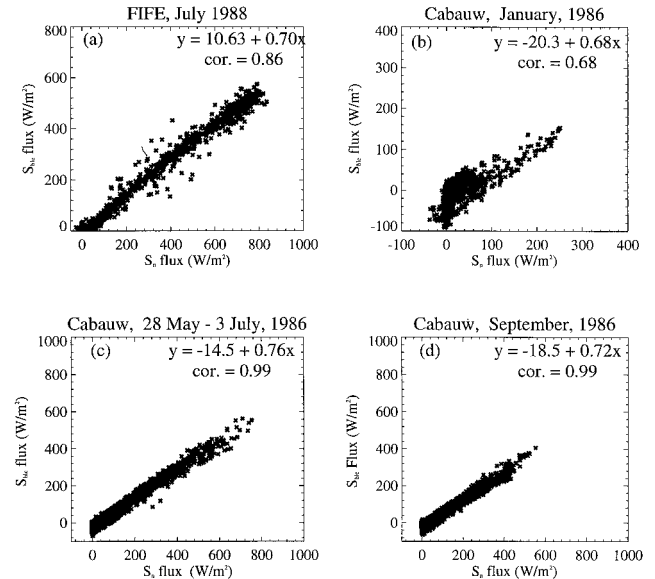


**Figure 6.** (a)  $F_n$  versus  $S_n$  of Desert Rock station measurement on a single day in July and (b) daily variations of  $F_n$  and  $S_n$ .

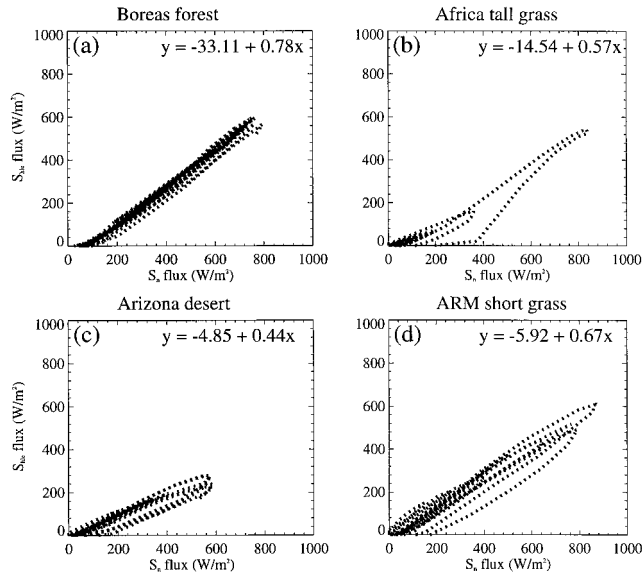


**Figure 7.** Relationships between net longwave radiation and net solar radiation over (a) BOREAS (54°N, 106°E), (b) Africa tall grass (15.5°N, 5.6°E), (c) Arizona desert (32°N, 109°E), and (d) ARM/CART shortgrass (36.61°N, 97.48°W), respectively. The data are from SCCM simulations for July. The linear regression formula is given at the top right-hand corner of each panel.

observations are from the FIFE field experiment in July 1988. The selected local time is 1000 LT, which matches one of the passing times of some polar orbiting satellites. The solid line in Figure 10a is the algorithm-produced skin temperature of  $T_s^{i(t)}$ , using (37) and measurements from the previous 2-day measurements. The dashed line is the ground-observed skin temperature for  $T_s^{i(t)}$ . The solid line in Figure 10b is also the calculated  $T_s^{i(t)}$  but using (38), i.e., without any flux corrections. The dashed line in Figure 10b is the same as that in



**Figure 8.** (a) Net  $S_{hle}$  flux versus net solar radiative flux ( $S_n$ ) over FIFE area for July 1988. The data include all hourly measurements for site-averaged FIFE observations. (b, c, d) Same as Figure 8a but from Cabauw experiment for different months in 1986.



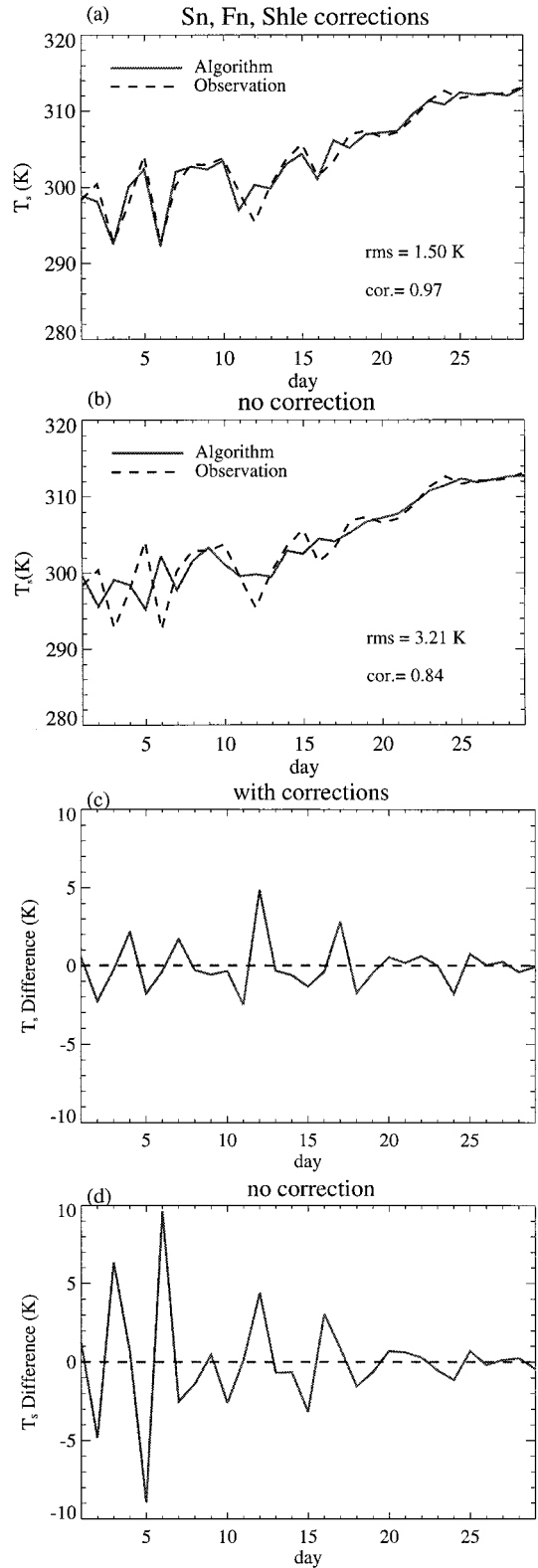
**Figure 9.** Relationship between  $S_{hle}$  fluxes and net solar radiation over Africa, Arizona, ARM/CART, and BOREAS forest, respectively. The data are from SCCM simulations for July. A linear regression formula is given at the top right-hand corner of each panel.

Figure 10a. Comparing Figures 10a and 10b illustrates the necessity of flux corrections during the daylight hours: the rms error reduces from 3.21 K to 1.50 K when the flux corrections are used. Figures 10c and 10d are  $\delta T_s^{i(t)}$ , the calculated  $T_s^{i(t)}$  minus the observed  $T_s^{i(t)}$ , for Figures 10a and 10b, respectively. The large disagreement for day 12 in Figure 10c is a result of the large cloud amount. Similar analyses are also conducted at 1400 LT (not shown). The “no-correction” treatment results in a rms error of 2.96 K for 1400 LT, while “with flux corrections”, the rms error reduces to 1.73 K. These numbers indicate the important influence of the flux on the surface temperature. This is because clouds modify the surface energy budget and, consequently, change the surface temperature. The significant improvement of accuracy is due to the flux correction term, as shown in (39). During daylight hours,  $\Delta S_n$ ,  $\Delta F_n$ , and  $\Delta S_{hle}$  are evident and thus result in adequate corrections.

Since there is no solar radiation at night, the skin temperature of a cloudy pixel is modified only through the net longwave radiation and the heat fluxes. Figure 11 compares algorithm-calculated skin temperature with ground-truth data at 2200 LT. Figures 11a and 11b show similar rms because of the small magnitudes of  $F_n$  and  $S_{hle}$  at night. Figures 11c and 11d show the departures of calculated skin temperature from the observations.

Figure 12 examines the detailed variations of  $S_n$ ,  $F_n$ , and  $S_{hle}$  and their influences on skin temperature. The data have half-hour intervals. The Julian day 198 was a cloudy day, and its previous day was a clear day. Figure 12a is the diurnal cycle of net solar radiation for the clear and cloudy days. Figures 12b and 12c are the net longwave radiation and the sum of sensible and latent heat fluxes, respectively. There was precipitation in the late afternoon of the cloudy day, as shown in Figure 12d. Figure 12e is the ground-truth skin temperature. The algorithm-calculated cloudy-day skin temperature is shown in Figure 12f, compared with the observed skin temperature. The calculation is conducted using the previous clear-day skin tem-

### Cloudy-algorithm, FIFE, July 1988, 1000LT



**Figure 10.** Comparison of algorithm-produced skin temperature with FIFE observations. The FIFE data are for each day in July 1988. Different treatments are described in the text: (a) full corrections and (b) no corrections. (c, d) Same as Figures 10a and 10b except for the temperature difference between algorithm-produced  $T_s$  and ground truth. Local time is 1000. See text for detail.

Cloudy-algorithm, FIFE, July 1988, 2200LT

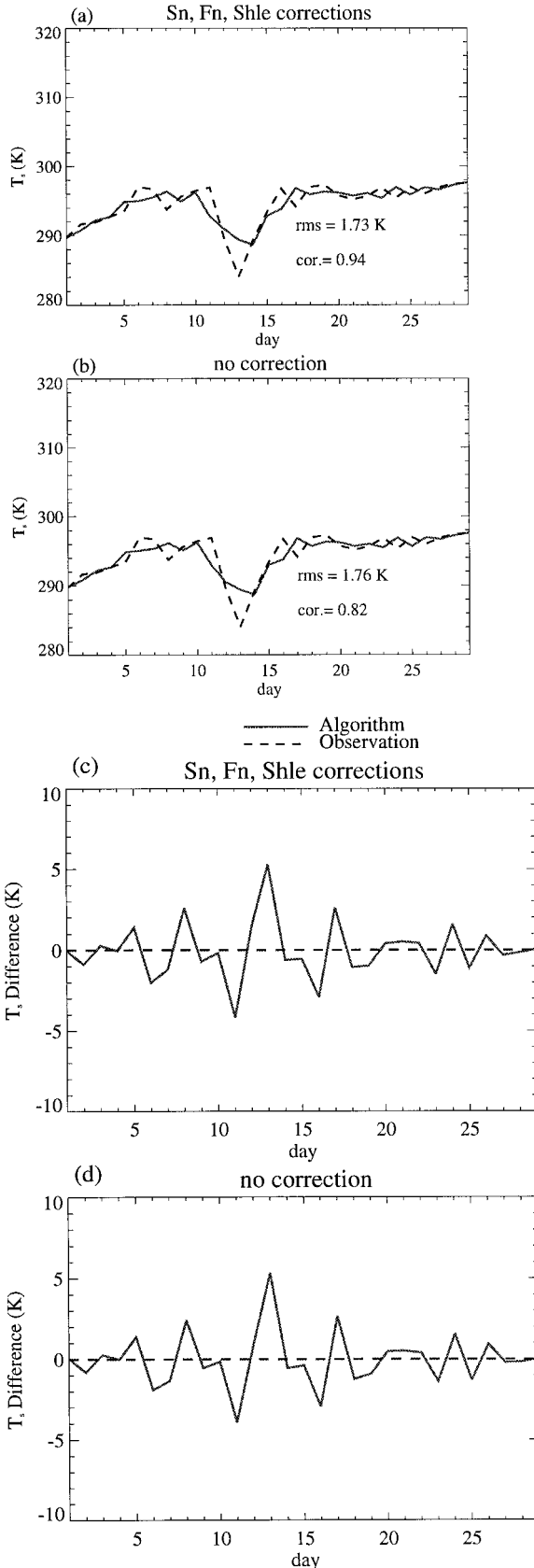


Figure 11. Same as Figure 10 except for the local time 2200.

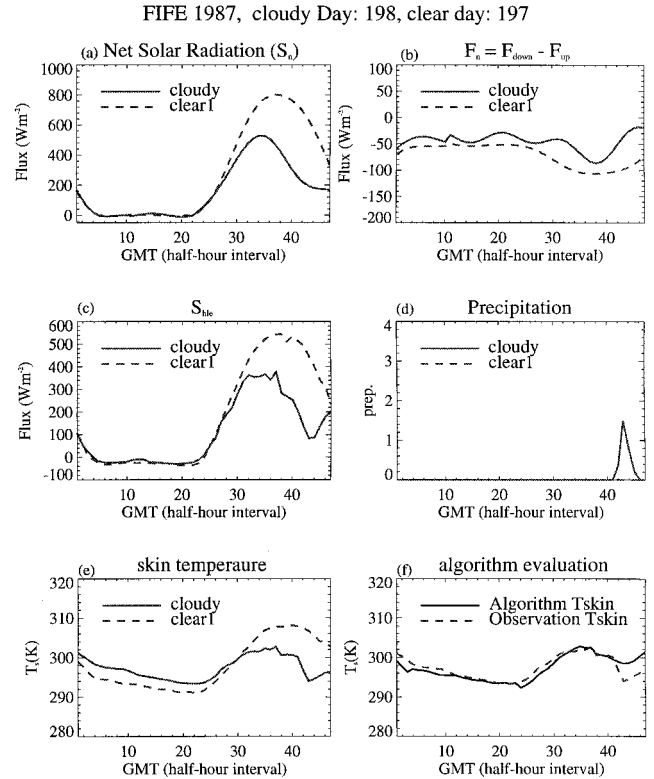


Figure 12. Detailed examinations of neighboring-pixel approach for a cloudy day in FIFE.

perature and the net solar radiation difference between these two days. The algorithm produces skin temperatures close to the observations but fails to predict the correct skin temperature for the time of precipitation.

The accuracy of the neighboring-pixel approach varies with season and with surface type. Figures 13 and 14 are for BOREAS forests in January and September 1996, representing the winter and fall seasons. The ground-truth data originally have 15-min intervals and now are sampled into a half hour. Two BOREAS observing stations are used: one at Prince Albert National Park and the other at Flin Flon. The measurements are sampled when Prince Albert was cloudy and Flin Flon was clear. In Figure 13a the x-coordinate axis is the ground-observed  $T_s^{i(t)}$  for Prince Albert, and the y-coordinate axis is the calculated  $T_s^{i(t)}$  using (37) with spatial neighboring pixels from Flin Flon and one previous-day measurement from Prince Albert. The rms error and correlation coefficients are given at the corner of the figure. Figure 13b is the  $\delta T_s^{i(t)}$ , which is the calculated  $T_s^{i(t)}$  minus the observations. Figure 14 is the same as Figure 13 except for September. The rms is 2.08 K for January and 1.87 K for September, with correlation coefficients as high as 0.99 and 0.96, respectively. Figure 13b and 14b show the temperature differences between algorithm-produced  $T_s$  and the ground truth, which, in general, are as much as 2 K. However, there are extreme cases with differences up to 8–10 K. Further analyses show that such large disagreements may be caused by strong convection systems and usually occur with heavy precipitation in the cloudy pixel.

**5.1.2. Model simulations.** Although the field experiments are carefully designed, the complexity of the surface is unlikely to be fully represented by these field experiments, which are

## Algorithm evaluation for BOREAS, January 1996

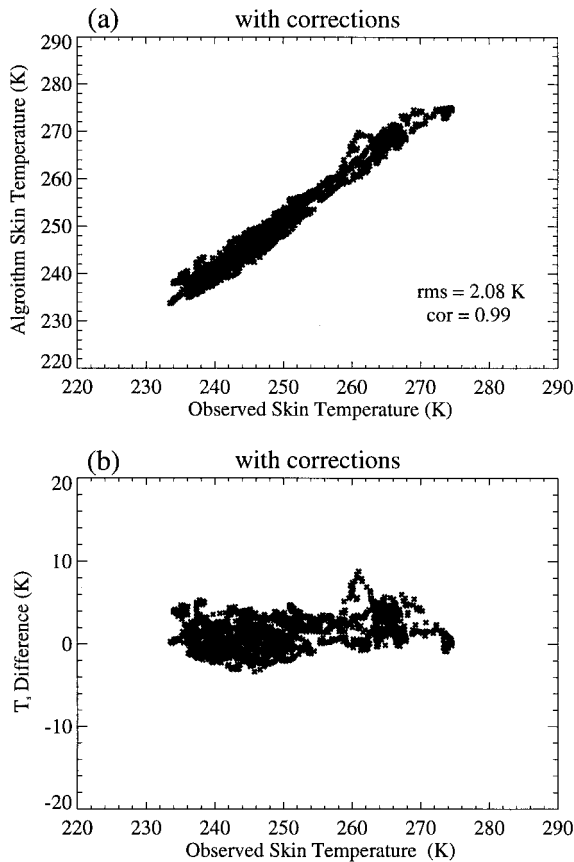


**Figure 13.** Algorithm evaluation for BOREAS area. Data are from the BOREAS field experiment in January 1996. The two measurement stations are Prince Albert and Flin Flon. The interval for measurements is 30 min. (a) Algorithm-produced  $T_s$  versus observations and (b) departures of algorithm-produced  $T_s$  from observations.

limited by the coverages, spatial and temporal resolutions, and surface variations. To examine the algorithm over other surface types, the GCM model is an essential research tool. Figure 15 is based on hourly CCM3/BATS simulation for July as described by *Jin and Dickinson* [1999]. Two pixels with a vegetation type of “crop/mixed farming” within 40°–45°N latitude band were selected. The data sampled for evaluation are taken when one grid is cloudy and the other is clear. Figure 15 is the algorithm-produced skin temperature (using (37)) versus the original CCM3-BATS-simulated skin temperatures for daylight hours and night hours, respectively. During the daytime the accuracy of the NP approach is about 1.23 K, while during the night, the accuracy is 1.21 K.

The properties of  $S_{hle}$ ,  $F_n$  (Figure 16a) and the sum of  $F_n$ ,  $S_{hle}$  (Figure 16b) at night are analyzed. At night the sign of  $S_{hle}$  is almost monotonically opposite to that of  $F_n$ , and the magnitudes of both fluxes are almost the same except when rain occurs. The sum of  $F_n$  and  $S_{hle}$ , as presented in Figure 16b, is as small as 20–40  $\text{W m}^{-2}$ , indicating the small exchanges of energy from soil to the surface and atmosphere. This further implies that at night the correction terms in (37) may cancel each other. This explains why the no-correction

treatment at night behaves similarly to the full correction treatment in Figure 11.

5.2.  $T_a$  Adjustment

Surface measurements of the 1996 BOREAS experiment [*Sellers et al.*, 1997] are used here to compare the  $T_a$ -adjustment-derived skin temperatures with the measured skin temperatures. Figure 17 shows one cloudy day (day 192) in July 1996 over the BOREAS. The calculated skin temperature is very close to the ground truth of  $T_s$ . The largest difference is less than  $\sim 1$  K for daytime, when the surface is less stable. At night the skin temperature is close to the air temperature because the surface layer is almost isothermal due to the energy exchanges.

## 6. Error Analysis

The algorithm uncertainties resulting from the satellite measurements and the model simulations are important, but discussions on how to reduce them are beyond the scope of this paper. In this section, the major error sources associated with the NP algorithm itself are analyzed. Note that the results shown here also include the contributions from uncertainties in the data measurement and errors introduced by the method used in the analysis.

## Algorithm evaluation for BOREAS, September 1996

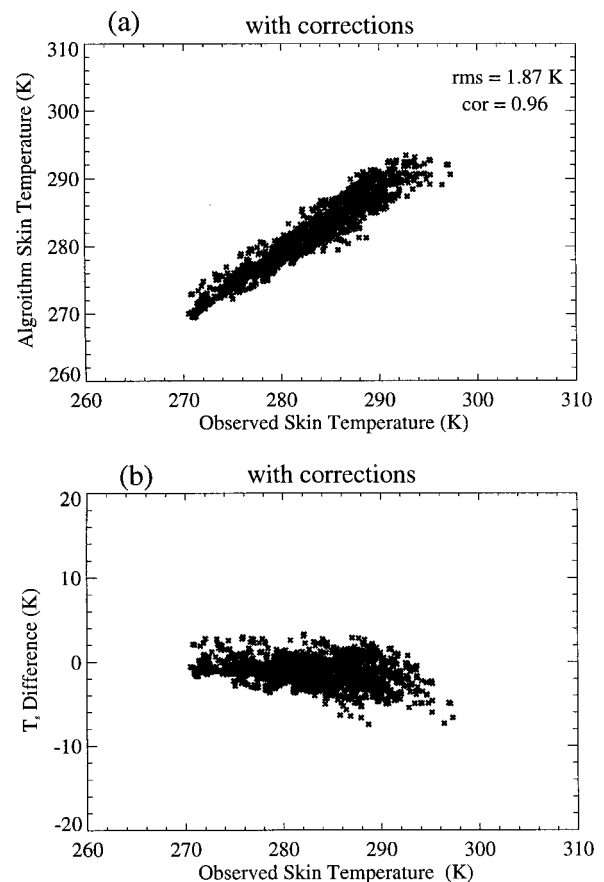


**Figure 14.** Same as Figure 13 except for September.

6.1. *K* Effects

*K* reflects the influences of vegetation type, soil type, and soil moisture on  $T_s$ . The physical meaning of *K* is the ratio of solar radiation change and  $T_s$  change. The empirical calculation method described earlier to derive *K* possibly causes uncertainty because it is originally inferred from small experimental areas [Dickinson *et al.*, 1993]. Figure 18 plots *K* against rms error for the algorithm-produced  $T_s$ , using (37), between ground observations at Prince Albert and Flin Flon. The rms errors vary by month, with the worst case being 2.6 K in July and the best case being 1.8 K in August and September. Obviously, the accuracy of the NP algorithm is sensitive to small *K* but varies only slightly for large *K*. This is because, as (37) illustrated, when *K* is large enough, the flux correction term is small. Therefore appropriate *K* can reduce the rms error. For example, with a typical *K* as  $140 \text{ W m}^{-2} \text{ K}^{-1}$  the rms is a minimum.

For areas where the ground heat flux is negligible, *K* is obtained from observations rather than from the suggested calculations because of some physical concerns. *K* for BOREAS is calculated from the BOREAS field experiment.

CCM3/BATS, July, 40-45N, Crop/mixed farming

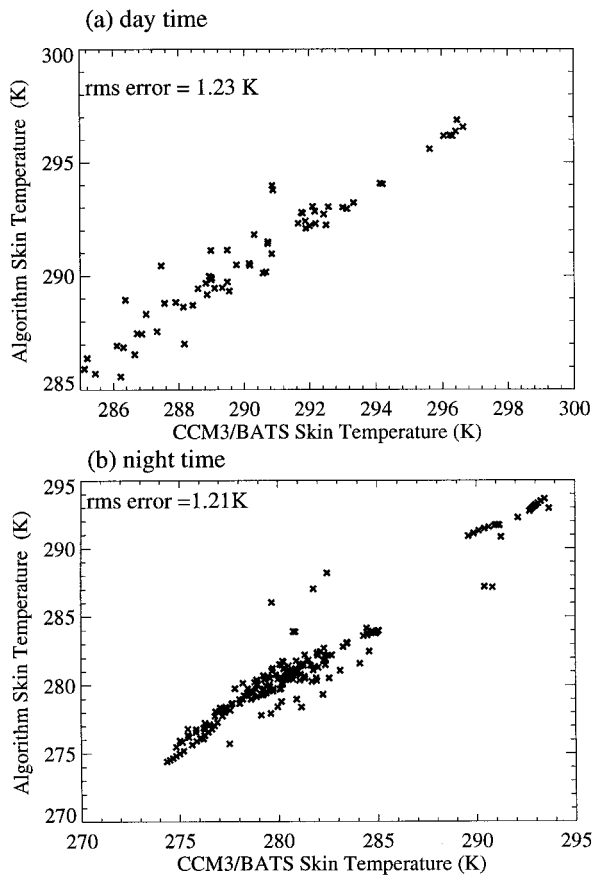


**Figure 15.** Comparison of algorithm-produced skin temperature with hourly CCM3/BATS simulations. The two grids with vegetation type as crop/mixed farming are selected for 40°–45°N. (a) All daylight hours when one pixel is cloudy but another is clear and (b) same as Figure 15a except for nighttime hours (rms errors are given for each treatment described in the text).

CCM3/BATS, July, 40-45N, Crop/mixed farming

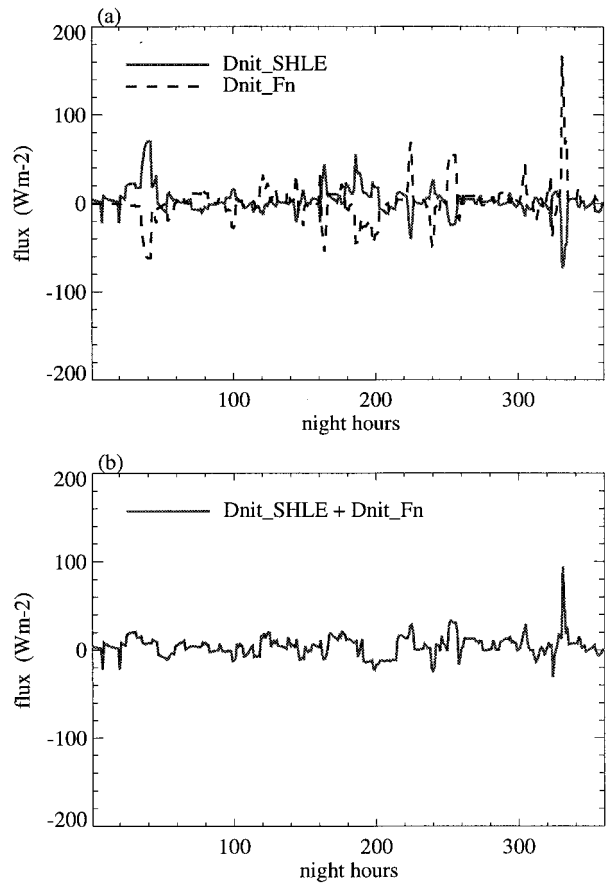


**Figure 16.** (a) Comparison of the nighttime  $\Delta S_{hle}$  and  $\Delta F_n$  between the two CCM3/BATS grids as used in Figure 8. “Dnit\_SHLE” stands for  $\Delta S_{hle}$  and “Dnit\_Fn” for  $\Delta F_n$ . (b) Sum of  $\Delta S_{hle}$  and  $\Delta F_n$ .

The validity of this value for other forest areas, in particular, tropical forest, must be determined before our algorithm can be applied over those areas. Since there are not enough measurements over the tropical forest, the climate model, CCM3/BATS, is used to examine *K* based on the physical consistency

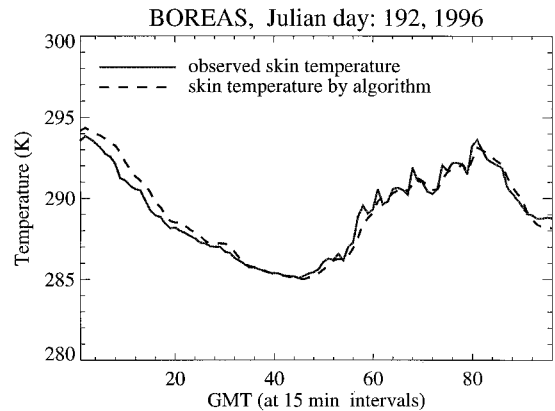


**Figure 17.** Examination of the  $T_a$  adjustment. The calculated skin temperature (dashed line) is based on the method described in section 3.2. The observations (solid line) are from BOREAS day 192 of 1996.

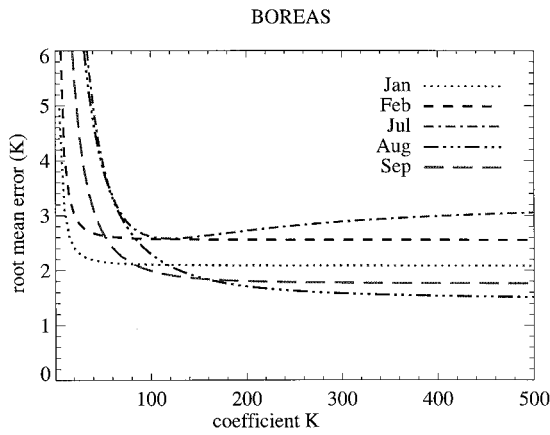


**Figure 18.** Effects of  $K$  versus rms error for the algorithm-produced  $T_s$ , using equation (37), between ground observations at Prince Albert and Flin Flon.

of the model. Figure 19 compares  $K$  for the boreal and Amazon forests. Although the rms error of the algorithm between temperate and tropical forests is different, the minimum rms is found at approximately the same  $K$ . This suggests that  $K$  is the same for temperate and tropical forests.

### 6.2. $F_n$ and $S_{hle}$ Effects

$S_{hle}$  and  $F_n$  cannot, from the foreseeable future, be obtained from satellite remote sensing. Parameterizing  $F_n$  and  $S_{hle}$  using  $\Delta S_n$ , suggested in (34) and (36), may cause errors. Figure 20 is the same as Figure 10 except that Figure 10 uses the observed  $\Delta S_n$ ,  $\Delta F_n$ , and  $\Delta S_{hle}$ , and Figure 20 uses parameterized  $\Delta F_n$  and  $\Delta S_{hle}$ . The reduction of accuracy in terms of rms is from 1.50 to 1.96 K, indicating that the error is caused by using statistical relationships to describe each day's surface longwave and heat fluxes. However, since the influences of  $F_n$  and  $S_{hle}$  are moderate compared to those of  $S_n$ , with the knowledge of  $S_n$  and the statistical relationships of  $F_n$  and  $S_{hle}$ , this parameterization provides an adequate  $T_s$  calculation to 1–2 K.

### 6.3. $S_n$ Effects

$S_n$  itself cannot be directly measured from satellites but can be derived from satellite-based measurements. Currently, accepted methods calculate  $S_{\downarrow}$  from the reflected solar radiation at the top of atmosphere (TOA). These methods usually use radiative transfer models and treat  $S_{\downarrow}$  as a function of pre-

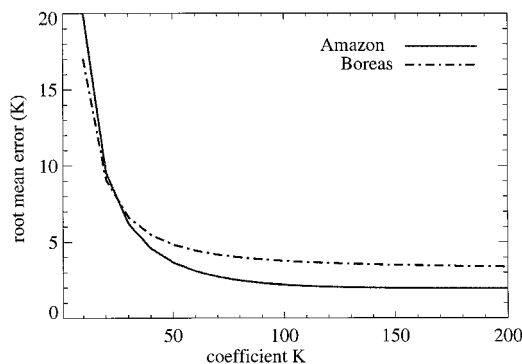


**Figure 19.** Comparison of  $K$  for BOREAS and the Amazon.

cipitable water, cloud conditions, and solar zenith angle [Pinker and Ewing, 1985; Li *et al.*, 1993]. Currently, the accuracy of such a method is about  $10 \text{ W m}^{-2}$  for monthly mean [Li *et al.*, 1993] and as much as  $30 \text{ W m}^{-2}$  or more at daily pixel resolution (Z. Li, personal communication, 1998). Instrument noise and atmospheric effects may reduce the retrieval accuracy of  $S_n$  at surface. The error of  $S_n$  is contributed by two parts: random error and systematic error. The latter is most likely the same for different pixels. Since our algorithm needs  $\Delta S_n$  between clear and cloudy pixels, the systematic error part can be largely, if not completely, removed. Therefore relatively poor absolute accuracy but relatively high accuracy of  $S_n$  is acceptable. Thus relative large  $S_n$ -related uncertainty becomes less significant when only the difference of  $S_n$ , rather than the absolute value, is used.

### 6.4. $T_s^{\text{clr}}$ Effects

$T_s^{\text{clr}}$  depends on the accuracy of  $T_s^{\text{clr}}$ . Poor absolute accuracy of a clear-pixel  $T_s$  will affect the absolute accuracy of the cloudy-pixel  $T_s$ .  $T_s^{\text{clr}}$  is generally determined by the split-window algorithm assuming that the atmospheric absorption can be approximated as a linear combination of the radiances measured at two different wavelengths [Sobrino *et al.*, 1994]. Currently, the best accuracy that land surface skin temperature product can have is 1 K in monthly level.

## 7. Summary

To calculate skin temperature for a satellite cloudy pixel, a cloudy-pixel treatment is developed as a hybrid technique of the neighboring-pixel approach and  $T_a$  adjustment. This algorithm has been examined against field experiments and CCM3/BATS simulations. The general accuracy of this algorithm is 1–2 K at monthly mean, pixel level. Despite the uncertainty in the algorithm, this work, for the first time, provides a useful guideline for calculating  $T_s$  from satellite data for cloudy pixels.

The physically meaningful neighboring-pixel approach is the main part of this work. This approach is from the surface energy balance equation. The basic concept of this approach is that for two neighboring pixels, which have similar surface properties, the temperature difference is due to the differences in energy fluxes, i.e., net solar radiation ( $\Delta S_n$ ), net longwave radiation ( $\Delta F_n$ ), and sensible and latent heat fluxes ( $\Delta S_{hle}$ )

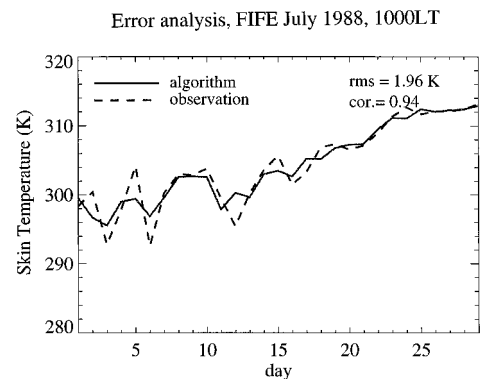


**Figure 20.** Effects of uncertainty caused by the parameterization of  $\Delta F_n$  and  $\Delta S_{hle}$ . Data are from FIFE July 1988. Local time is 1000. The algorithm-produced skin temperature is compared with observations. The  $\Delta F_n$  and  $\Delta S_{hle}$  are calculated from the regression equations obtained in Figures 5 and 8.

between the cloudy and its neighboring pixels. Such radiation and heat flux differences mainly result from cloud cover. With this understanding, the cloudy-pixel skin temperature can be calculated using the temperature of neighboring clear pixels and surface energy distribution,  $\Delta S_n$ ,  $\Delta F_n$ , and  $\Delta S_{hle}$ . The latter two terms,  $\Delta F_n$  and  $\Delta S_{hle}$ , are not available from satellites and thus need to be parameterized to  $\Delta S_n$  for daytime. The preceding results establish that the accuracy of this algorithm is about 1.5–2.5 K for monthly mean pixel level resolution.

During the daytime, difference in the net solar radiation between the neighboring pixels is the primary reason for their surface temperature differences, if the neighboring pixels are defined as having similar surface and soil properties. At night, however, the temperature difference is caused by energy exchange among heat fluxes, longwave flux, and ground flux. The cloudy-pixel skin temperature is close to its 2-m air temperature because of the stability of the surface layer.  $\Delta S_{hle}$  and  $\Delta F_n$  between a cloudy pixel and its neighboring clear pixel almost compensate for each other except for nights with heavy precipitation.

The NP approach has less error for daylight hours than for nights and rainfall cases. An additional  $T_{air}$  adjustment is designed on the basis of the boundary layer theory and can calculate the skin temperature from the surface air temperature. This method, although having accuracy of 1 K in large cloud coverage and night cases, suffers from surface heterogeneity. Thus it can be applied only to small areas where surface observations are available or areas where surface is relatively homogeneous.

The relationships between variations of net radiation and skin temperature are examined with FIFE and BOREAS field experiments. Consistent with earlier studies, surface skin temperature depends heavily on radiation reaching the surface. For forest areas the sensitivity of skin temperature to radiation is about 0.007 K W m<sup>-2</sup>. This value seems not to vary significantly with latitude and season.

## Appendix

From the boundary layer Monin-Obukhov similarity theory for the potential temperature profile [Garratt, 1992, chapter 3],

$$\Theta_v - \Theta_0 = \frac{\Theta_*}{k} \left[ \ln \left( \frac{Z}{Z_{or}} \right) - \Psi_H(\zeta) \right], \quad (26)$$

$$U = \frac{U_*}{k} \left[ \ln \left( \frac{Z}{Z_0} \right) - \Psi_M(\zeta) \right], \quad (27)$$

$$L = \frac{-U_*^3 \Theta_0}{gk \Theta_* U_*}, \quad (28)$$

$$\Theta_0 = T_0 \left( \frac{1000}{P_0} \right)^{R/c_p}, \quad (29)$$

where  $\Theta_0$  is the surface potential temperature at  $T_0$ ,  $T_0$  is the absolute surface temperature,  $L$  is the Obukhov length, and  $Z_{or}$  is the surface roughness scaling length for temperature (related to the aerodynamic roughness length).  $P_0$  is surface pressure,  $R$  is the gas constant, and  $c_p$  is the specific heat at constant pressure. At  $Z_{or}$ ,  $T_0$  is the actual skin temperature  $T_s$ .  $Z_0$  is aerodynamic roughness length and usually is an order of magnitude greater than  $Z_{or}$ .  $\Theta_* = -(\text{SH}/\rho c_p U_*)$ ,  $k = 0.4$ .

For unstable conditions:  $\zeta = Z/L < 0$ ,

$$\Psi_M(\zeta) = 2 \ln \left[ \frac{1+x}{2} \right] + \ln \left[ \frac{1+x^2}{2} \right] - 2 \tan^{-1} x + \frac{\pi}{2}, \quad (30)$$

$$\Psi_H(\zeta) = 2 \ln \left[ \frac{1+y}{2} \right], \quad (31)$$

$$x = (1 - \gamma_1 \zeta)^{-1/4}, \quad (32)$$

$$y = (1 - \gamma_2 \zeta)^{-1/2}. \quad (33)$$

For stable conditions where  $\zeta = Z/L \geq 0$ ,

$$\Psi_M(\zeta) = \Psi_H(\zeta) = \beta_1 \zeta, \quad (34)$$

with  $\gamma_1 \approx \gamma_2 \approx 16$  and  $\beta_1 \approx 5$ .

However, since there are five unknown variables,  $\Theta_0$ ,  $T_0$ ,  $U_*$ ,  $\Theta_*$ , and  $L$ , in the four equations (26), (27), (28), and (34) for cloudy cases, it is important to solve the closure problem with one of the well-accepted assumptions; that is, according to the relationships between stability parameters and estimations of  $L$ , one can determine  $L$  based on wind, cloud amount, precipitation, and atmospheric stability. Research shows that the surface layer is generally neutral under radiative-significant cloudy sky, and its  $L$  is close to 0.25 [Panofsky and Dutton, 1984].

**Acknowledgments.** The author thanks the two anonymous reviewers for their professional comments. Thanks also go to R. E. Pickinon for his insightful discussions and financial support during this work. This work is supported by NASA graduate student fellowship and by the NASA EOS Interdisciplinary Scientific Research Program (U.P.N. 429-82-22; U.P.N. 428-81-22).

## References

- Bastable, H. G., W. J. Shuttleworth, R. L. G. Dallarosa, G. Fisch, and C. A. Nobre, Observations of climate, albedo, and surface radiation over cleared and undisturbed Amazonian forest, *Int. J. Climatol.*, **13**, 783–796, 1993.
- Beljaars, A. C. M., and P. Bosveld, The sensitivity of winter evaporation to the formulation of aerodynamic resistance in the ECMWF model, *Boundary Layer Meteorol.*, **71**, 135–149, 1994.
- Becker, F., and S.-L. Li, Temperature-independent spectral indices in thermal infrared bands, *Remote Sens. Environ.*, **32**, 17–33, 1990.
- Betts, A. K., and J. H. Ball, The FIFE surface diurnal cycle climate, *J. Geophys. Res.*, **100**, 25,679–25,693, 1995.
- Betts, A. K., J. H. Ball, A. C. M. Beljaars, M. J. Miller, and P. A. Viterbo, The land surface-atmosphere interaction: A review based on observational and global modeling perspectives, *J. Geophys. Res.*, **101**, 7209–7225, 1996.
- Cess, R. D., Climate change: An appraisal of atmospheric feedback mechanisms employing zonal climatology, *J. Atmos. Sci.*, **33**, 1831–1843, 1976.
- Cess, R. D., et al., Interpretation of climate feedback as produced by 24 stratospheric general circulation models and produced by 14 atmospheric general circulation models, *Science*, **245**, 513–516, 1989.
- Deardorff, J. W., Efficient prediction of ground surface temperature and moisture, with inclusion of a layer of vegetation, *J. Geophys. Res.*, **83**, 1889–1903, 1978.
- Dickinson, R. E., The force-restore model for surface temperatures and its generalization, *J. Clim.*, **1**, 1086–1097, 1988.
- Dickinson, R. E., A. Henderson-Sellers, and P. J. Kennedy, Biosphere-Atmosphere Transfer Scheme (BATS) Version 1E as coupled to the NCAR community climate model, *NCAR Tech. Note, NCAR/TN-387+STR*, pp. 72, Natl. Cent. for Atmos. Res., Boulder, Colo., 1993.
- Garratt, J. R., *The Atmospheric Boundary Layer*, chap. 3, Cambridge Univ. Press, New York, 1992.
- Garratt, J. R., Observed screen (air) and GCM surface/screen temperatures: Implications for outgoing longwave fluxes at the surface, *J. Clim.*, **8**, 1360–1368, 1995.

- Jin, M., R. E. Dickinson, and A. M. Vogelmann, A comparison of CCM2/BATS skin temperature and surface-air temperature with satellite and surface observations, *J. Clim.*, *10*, 1505–1524, 1997.
- Jin, M., and R. E. Dickinson, Interpolation of surface radiation temperature measured from polar orbiting satellites to a diurnal cycle, 1, Without clouds, *J. Geophys. Res.*, *104*, 2105–2116, 1999.
- Li, Z., H. G. Leighton, K. Masuda, and T. Takashima, Estimation of SW flux absorbed at the surface from TOA reflected flux, *J. Clim.*, *6*, 317–330, 1993.
- Lian, M. S., and R. D. Cess, Energy balance climate models: A reappraisal of ice-albedo feedback, *J. Atmos. Sci.*, *34*, 1058–1062, 1977.
- Minnett, P. J., Consequences of sea surface temperature variability on the validation and applications of satellite measurements, *J. Geophys. Res.*, *96*, 18,475–18,489, 1991.
- Minnis, P., and E. F. Harrison, Diurnal variability of regional cloud and clear-sky radiation parameters derived from GOES data, part I, Analysis method, *J. Climatol. Appl. Meteorol.*, *23*, 993–1011, 1984.
- Minnis, P., P. W. Heck, and E. F. Harrison, The 27–28 October 1986 FIRE IFO Cirrus Case Study: Cloudy parameter fields derived from satellite data, *Mon. Weather Rev.*, *118*, 2426–2447, 1990.
- Ockert-Bell, M. E., and D. L. Hartmann, The effect of cloud type on Earth's energy balance: Results from selected region, *Bull. Am. Meteorol. Soc.*, *5*, 1157–1171, 1992.
- Panofsky, H. A., and J. A. Dutton, *Atmospheric Turbulence: Models and Methods for Engineering Applications*, Wiley-Interscience, New York, 1984.
- Parata, A. J., V. Caselles, C. Colland, J. A. Sobrino, and C. Ottle, Thermal remote sensing of land surface temperature from satellites: Current status and future prospects, *Remote Sens. Rev.*, *12*, 175–224, 1995.
- Pinker, R. F., and J. A. Ewing, Modeling surface solar radiation: Model formulation and validation, *J. Climatol. Appl. Meteorol.*, *24*, 389–401, 1985.
- Price, J. C., Land surface temperature measurements from the split window channels of the NOAA-7 advanced very high resolution radiometer, *J. Geophys. Res.*, *89*, 7231–7237, 1984.
- Ramanathan, The role of Earth radiation budget studies in climate and general circulation research, *J. Geophys. Res.*, *92*, 4075–4095, 1987.
- Randall, D., and B. A. Wielicki, Measurements, models, and hypotheses in the atmospheric sciences, *Bull. Am. Meteorol. Soc.*, *78*, 399–406, 1997.
- Sellers, P. J., F. G. Hall, G. Asrar, D. E. Strebel, and R. E. Murphy, An overview of the First International Satellite Land Surface Climatology Project (ISLSCP) Field Experiment (FIFE), *J. Geophys. Res.*, *97*, 18,345–18,371, 1992.
- Sellers, P. J., et al., The Boreal Ecosystem-Atmosphere Study (BOREAS): An overview and early results from the 1994 field year, *Bull. Am. Meteorol. Soc.*, *76*, 1549–1577, 1995.
- Sellers, P. J., et al., BOREAS in 1997: Experiment overview, scientific results, and future directions, *J. Geophys. Res.*, *102*, 28,731–28,769, 1997.
- Shuttleworth, W. J., Micrometeorology of temperature and tropical forest, *Philos. Trans. R. Soc. London, Ser. B*, *324*, 299–334, 1989.
- Sobrino, J. A., Z.-L. Li, M. P. Stoll, and F. Becker, Improvements in the split-window technique for land surface temperature determination, *IEEE Trans. Geosci. Remote Sens.*, *32*(2), 243–253, 1994.
- Stull, R. B., *An Introduction to Boundary Layer Meteorology*, 670 pp., Kluwer Acad., Norwell, Mass., 1988.
- Wan, Z., and J. Dozier, A generalized split-window algorithm for retrieving land-surface temperature from space, *IEEE Trans. Geosci. Remote Sens.*, *34*, 892–905, 1996.

---

M. Jin, Laboratory of Global Remote Sensing, Department of Geography, University of Maryland, 2181 LeFrank Hall, College Park, MD 20742. (menglin@atmo.arizona.edu)

(Received March 12, 1999; August 20, 1999; accepted August 26, 1999.)